Title	Performance of leading artifact removal algorithms assessed across microwave breast imaging prototype scan configurations
Author(s)	Elahi, Muhammad Adnan; Curtis, C.; Lavoie, B.R.; Glavin, Martin; Jones, Edward; Fear, E.; O'Halloran, Martin
Publication Date	2017-03-02
Publication Information	Elahi, M. A., Curtis, C., Lavoie, B. R., Glavin, M., Jones, E., Fear, E., & O'Halloran, M. (2017). Performance of leading artifact removal algorithms assessed across microwave breast imaging prototype scan configurations. Computerized Medical Imaging and Graphics, 58(Supplement C), 33-44. doi: https://doi.org/10.1016/j.compmedimag.2017.02.003
Publisher	Elsevier
Link to publisher's version	https://doi.org/10.1016/j.compmedimag.2017.02.003
Item record	http://hdl.handle.net/10379/7032
DOI	http://dx.doi.org/10.1016/j.compmedimag.2017.02.003

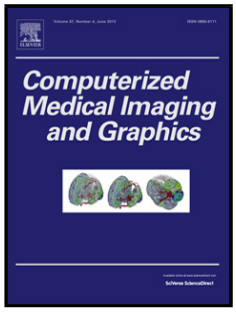

Title: Performance of Leading Artifact Removal Algorithms Assessed Across Microwave Breast Imaging Prototype Scan Configurations

Author: M.A. Elahi C. Curtis B. Lavoie M. Glavin E. Jones E. Fear M. O'Halloran

PII: S0895-6111(17)30010-1
DOI: http://dx.doi.org/doi:10.1016/j.compmedimag.2017.02.003
Reference: CMIG 1497

To appear in: *Computerized Medical Imaging and Graphics*

Received date: 5-7-2016
Revised date: 1-2-2017
Accepted date: 27-2-2017

Please cite this article as: M.A. Elahi, C. Curtis, B. Lavoie, M. Glavin, E. Jones, E. Fear, M. O'Halloran, Performance of Leading Artifact Removal Algorithms Assessed Across Microwave Breast Imaging Prototype Scan Configurations, *<![CDATA[Computerized Medical Imaging and Graphics]]>* (2017), http://dx.doi.org/10.1016/j.compmedimag.2017.02.003

Performance of Leading Artifact Removal Algorithms Assessed Across Microwave Breast Imaging Prototype Scan Configurations

M. A. Elahi[a,*], C. Curtis[b], B. Lavoie[b], M. Glavin[a], E. Jones[a], E. Fear[b], M. O'Halloran[a]

[a] *Electrical and Electronic,National University of Ireland Galway*
[b] *Dept. of Electrical and Computer Engineering, University of Calgary, AB, Canada*

Abstract

Microwave imaging is a promising imaging modality for the detection of early-stage breast cancer. One of the most important signal processing components of microwave radar-based breast imaging is early-stage artifact removal. Several artifact removal algorithms have been reported in the literature. However, the neighbourhood-based skin subtraction and hybrid artifact removal algorithms have shown particularly promising results in different realistic 3D breast phantoms. For the first time in this paper, both algorithms have been evaluated and compared using the scan approaches of the most common microwave breast imaging prototype systems. The tests include 3D numerical as well as experimental breast phantoms scanned with hemispherical, cylindrical and adaptive scanning patterns. The efficacy of both algorithms has been evaluated across a range of appropriate performance metrics.

Keywords: Microwave Imaging, Ultra Wideband Radar, Breast Cancer, Artifact Removal, Skin Subtraction, Skin-Artifact Removal

1. Introduction

Most UWB radar-based systems for breast cancer detection include early-stage artifact removal and image reconstruction algorithms [1]. The early-stage artifact typically consists of the input signal, the reflection from the skin surface, skin-fat interface and any antenna reverberation present. This artifact is typically several orders of magnitude greater than the reflections from any tumours present within the breast. If the artifact is not removed effectively it could easily mask tumours at the image reconstruction stage.

A large number of early-stage artifact removal algorithms for microwave imaging of the breast have been reported in the literature [2, 3, 4, 5, 6, 7, 8].

*Corresponding author
Email address: m.elahi1@nuigalway.ie (M. A. Elahi)

A comprehensive comparison of various artifact removal algorithms has been presented in [9]. The study has shown that the average [3] and the rotation subtraction methods [5] do not work well due to normal variation between channel artifacts. Conversely, filter-based methods [4, 6] are more robust to the variation in between-channel artifacts, but the temporal window containing the artifact must be known *a-priori*. Estimation of the artifact-dominant time-window and the selection of appropriate channels to estimate the artifact is critical to the performance of filter-based algorithms. The entropy-based method [7] often fails to accurately estimate the time-window. It can also introduce distortion into the tumour response. This could produce false positives or mask the tumour in the image. The frequency domain method [8] also tends to distort the tumour response while removing the skin-artifact.

Two algorithms in particular have shown promising results: the Neighbourhood-based Skin Subtraction (NSS) [10]; and the Hybrid Artifact Removal (HAR) [11]. The NSS algorithm improves the filter-based method proposed in [6]. The NSS algorithm introduces a method to select a cluster of neighboring channels, around the target channel, to estimate the artifact in the target channel. Appropriate selection of the neighborhood improves the artifact estimation by using signals which are similar to the target signal. The NSS also introduces an automatic method to select the artifact-dominant portion of the signal for filter weight computation. The improvement in results has been demonstrated by applying the NSS algorithm to 3D numerical as well as to a simple experimental breast phantom and to patient data [10].

The HAR algorithm is another extension of the filter-based method. In the HAR algorithm, the artifact in a target signal is estimated as the filtered combination of the artifact in all other signals. The filter weights are optimized using an estimated artifact-dominant window. The HAR algorithm estimates the artifact-dominant portion of the signal using the entropy-based method described in [7]. The estimated time-window is then used as *a-priori* information for the computation of filter weights to estimate the artifact. The HAR algorithm uses the antennas exclusively located in the same z-plane as the target antenna for inclusion in the artifact estimation, in contrast to the neighbourhood-based approach used in NSS. The algorithm efficacy has been demonstrated using 3D anatomically and dielectrically realistic numerical breast models [11].

Both the NSS and the HAR algorithm overcome the limitations of the filter-based algorithm [6] by proposing methods to: estimate the artifact-dominant time-window; and select appropriate neighbouring antennas for the artifact estimation.

Both algorithms have shown promising results in 3D scenarios. However, they have been evaluated separately on different breast phantoms and different scan configurations. For the first time, this study aims to evaluate the efficacy of both algorithms using the same numerical as well as experimental breast phantoms scanned with different scan patterns:

- cylindrical;
- hemispherical;

- adaptive/patient-specific.

The cylindrical scan pattern is used in the Tissue Sensing Adaptive Radar (TSAR) prototype [12] that has also been used in a patient study [13]. Some of the other prototypes that use the cylindrical scan pattern are reported in [14, 15]. The hemispherical scan pattern is similar to the prototype system used in clinical trials reported in [16]. Another example of a prototype system that houses antennas in a hemispherical radome is described in [17]. The patient-specific scan pattern is used in the second generation TSAR prototype [18]. These different scan patterns facilitate the evaluation of the robustness of artifact removal algorithms against various scan configurations.

The various scan configurations also allow the generalizability of results across all microwave breast imaging prototype systems that use the monostatic data acquisition approach. Even though different prototypes use different hardware and in particular different antenna type, both algorithms can still be applied to the acquired data. This is due to the fact that the performance of both algorithms is effected by the placement of the antenna (scan pattern) and not by the antenna type used for the measurement. Both algorithms can potentially be adapted for the multistatic data which is more challenging than the monostatic data due to the variation of the early-stage artifact in multistatic signals.

The shape of two numerical breast phantoms has been constructed from laser data acquired during a patient study [13]. This presents a challenging scenario (i.e a realistic breast shape) for the artifact removal algorithms. The third numerical breast phantom has been derived from an MRI of a real patient and is representative of a realistic breast. The experimental breast phantoms have also been used to evaluate the performance of both algorithms in the presence of realistic noise. The experimental breast phantoms are created with dielectric properties close to those of human tissues for both skin and internal structures of the breast. The results have been compared using a range of appropriate signal and image quality metrics. Preliminary results were reported in [19].

The remainder of the paper is organised as follows: Section 2 describes each artifact removal algorithm in detail; Section 3 describes the imaging algorithm used in this study; the various simulated breast phantoms, experimental breast phantoms and the pre-processing steps applied to the data before imaging are covered in Section 4; Section 5 describes the performance metrics used to evaluate the algorithms; Section 6 presents the results and discussion; and finally the conclusions and suggestions for future work are discussed in Section 7.

2. Artifact Removal Algorithms

2.1. Hybrid Artifact Removal

2.1.1. Artifact Dominant Time-Window Estimation

The first step in the hybrid artifact removal algorithm [11] is to estimate the artifact-dominant portion of radar signals based on the entropy values. A larger value of entropy is obtained from similar artifacts in the early portion

of the radar signal and conversely the tumour reflections result in much lower entropy values. Next, a window function estimated to contain the artifact can be defined based on these entropy values.

The $\alpha - order$ Renyi entropy at time sample n is defined as:

$$H_\alpha[n] = \frac{1}{1-\alpha} log \left\{ \sum_{i=1}^{Q} (p_i[n])^\alpha \right\} \tag{1}$$

where $p_i[n]$ is the probability density function obtained by normalizing each radar signal $b_i[n]$, Q is the total number of channels, α is real-positive and the entropy varies from zero (for certain events) to $log\ Q$ for uniform distributions. In this study $\alpha = 3$ is used, as third-order entropy is typically defined for a broad class of signals [7]. Next, the theoretical dimension of $[b_1[n], b_2[n], ..., b_Q[n]]$ is defined as:

$$D[n] = e^{H_\alpha^s[n]} \tag{2}$$

where $H_\alpha^s[n]$ is the smoothed entropy.

In order to estimate the artifact-dominant time window, the maxima of the function $D[n]$ is computed (the first *maximum* represents the point in time where signals across all channels have highest similarity, and the adjacent local *minimum* indicates the maximum variation). The highly similar part of the signals is assumed to be the artifact. The artifact-dominant time window is then defined from the start of the signal to the local *minima* on the theoretical dimension curve.

2.1.2. Artifact Filtering

In this step, the artifact is removed by applying the Wiener Filter [6] over the artifact-dominant portion of the signal, at each channel, as computed in the previous step. The artifact in each channel is estimated as a filtered combination of the signals in all other channels. The estimated artifact signal for channel i is then subtracted from the received signal at channel i as follows:

$$s_i[n] = b_i[n] - q^T b_{PN}[n] \tag{3}$$

where $b_i[n]$ is the vector containing the signal received at channel i, $b_{PN}[n]$ is a vector calculated from all other channels located in same z-plane except i, and q is the vector of filter weights. For example, in order to remove the artifact from Channel 1, the filter weight vector is calculated as:

$$q = \arg\min_q \sum_{n=n_o}^{n_o+m-1} \left| b_1[n] - q^T b_{2N}[n] \right|^2 \tag{4}$$

where n_o represents the start of the signal and m is the length of the artifact-dominant portion of the signal, estimated as described in the previous subsection. The minimization problem of Eq. 4 is solved in a similar way to [6].

2.2. Neighbourhood-based Skin Subtraction Algorithm

2.2.1. Artifact-Dominant Window Selection

The NSS algorithm first processes backscattered radar signals collected at each channel through an artifact-dominant window selection algorithm. The undesired early-stage artifact tends to be several orders of magnitude larger than responses from internal structures, and can be isolated by finding maxima greater than a predetermined threshold value. The start of the artifact-dominant window (w_1) is set equal to the time step corresponding to the trough that precedes the first significant peak. The end of the artifact-dominant window (w_2) is defined as the time step corresponding to the trough that follows the last significant peak [10].

2.2.2. Neighbourhood Selection

The neighbouring channels of a target antenna are defined based on the antenna proximity and the cross-correlation between the recorded signals [10]. The reflections from each neighbouring antenna are then cross-correlated with the reflection from the target antenna to validate the similarity of reflections. Next, a pre-calculated threshold is used to validate the similarity of reflections from antennas included in the neighbourhood to the target antenna. Any antenna not meeting the similarity criteria is excluded. The similarity criteria ensures that antennas selected in the neighbourhood have enough similarity to provide an accurate estimate of the artifact in the target channel.

2.2.3. Artifact Filtering

The artifact filtering process is similar to the one described in Section 2.1.2. Eq. 3 is used to remove the artifacts from each channel i and rewritten as:

$$s_\tau[n] = b_\tau[n] - q^T b_{neighbours,\tau}[n] \tag{5}$$

where τ is the target antenna, $b_{neigbours,\tau}[n]$ is the combination of signals from neighbourhood antennas selected for the target antenna τ, and q are the filter weights. The filter weights are calculated as:

$$q = \arg\min_q \sum_{n=w_1}^{w_2} \left| b_\tau[n] - q^T b_{neighbours,\tau}[n] \right|^2 \tag{6}$$

where w_1 and w_2 are the start and end, respectively, of the artifact-dominant window calculated as explained in the previous subsection. Eq. 6 can be solved as described in [10].

3. Imaging

A Delay-And-Sum (DAS) imaging algorithm [13] is used to form the final breast images. The artifact-free backscattered radar signals are time-aligned,

summed and then squared for each synthetic focal point $\vec{r} = (x, y, z)$ within the breast. The 3D energy profile of the breast is created as follows:

$$I(\vec{r}) = \left[\sum_{i=1}^{M} b_i(\tau_i(\vec{r}))\right]^2 \tag{7}$$

where M is the total number of channels, b_i is the backscattered signal recorded at channel i, $\tau_i(\vec{r})$ is the time required to travel the round trip distance between focal point $\vec{r}$ and the channel i. $\tau_i(\vec{r})$ is dependent on the propagation speed of the electromagnetic wave. An average propagation speed is typically used to estimate $\tau_i(\vec{r})$. However, the propagation speed varies as the wave travels through the immersion medium, breast skin and the interior of the breast. Laser data collected during breast scanning is used to estimate the breast surface [20]. The outline of the breast is then used to estimate the distance travelled in the immersion medium, skin and the interior of the breast. This allows a more accurate estimation of $\tau_i(\vec{r})$ by using different propagation speeds corresponding to the distance travelled in each medium.

4. Breast Phantoms

4.1. Numerical Breast Phantoms

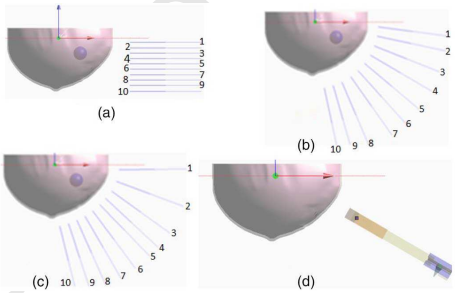

Figure 1: Large breast phantom and scan patterns, (a) Cylindrical, (b) Hemispherical, (c) Patient-specific, (d) Orientation of antenna corresponding to fourth position of hemispherical scan pattern (from [21])

Three numerical breast phantoms have been considered in this study. The laser data acquired in the patient study [13] (study E-22121 approved by the Conjoint Health Research Ethics Board, University of Calgary) has been used to reconstruct realistic skin surfaces for the first two breast phantoms. The mean skin thickness is 2mm and the internal breast tissues have been modeled as homogeneous fat. A 15mm diameter tumour is included in each breast phantom at different locations as described in Table 1.

The internal tissue structure of the first two breasts is modeled simplistically as opposed to using more realistic heterogeneous tissue structure. This is because this study aims to evaluate the performance of early-stage artifact

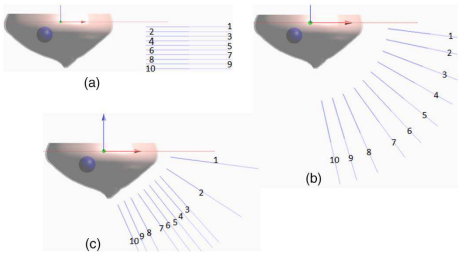

Figure 2: Small breast phantom and scan patterns, (a) Cylindrical, (b) Hemispherical, (c) Patient-specific (from [21])

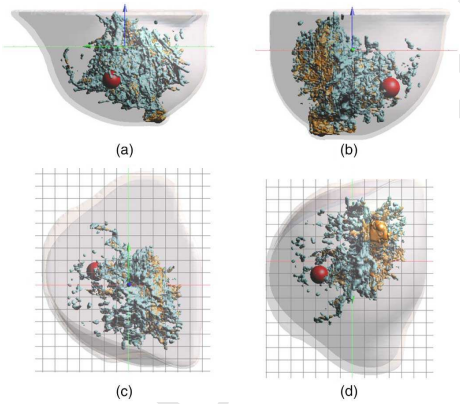

Figure 3: Heterogeneous breast phantom derived from an MR scan of a patient showing distribution of different breast tissues with (a) and (b) side, (c) top and (d) bottom views. Three different types of glandular tissues are shown in different colours (from [21]).

removal algorithms. The primary source of early-stage artifacts is the skin response. However, the quantification of clutter due to the early-stage artifacts in the images becomes ambiguous in the presence of heterogeneous breast tissues. In the absence of heterogeneous tissues, the clutter in the images can be attributed to the residual artifacts.

The challenge for artifact removal algorithms is the realistic variation in skin shape, curvature and thickness. The tumour located close to the skin also presents a challenge, as the tumour response may be embedded in the skin response and could be distorted by the artifact removal algorithm. Another issue is the various scan configurations. The breast phantoms used in this study have been designed taking these challenges into consideration. The third numerical breast phantom is derived from an MR scan of a patient and the interior is composed of fat as well as three different types of glandular tissue as shown in Fig. 3.

The breast phantoms are modelled as immersed in canola oil. The canola oil has shown to be an effective coupling medium for the microwave imaging

Table 1: Summary of numerical and experimental breast phantoms used in this study

Phantom Label	Phantom Type	Scan Configuration	Tumour Location	Tumour Size
C1	Homogeneous Small	Cylindrical	(-15, 0,- 12)	15mm
C2	Homogeneous Large	Cylindrical	(24, 3, -17)	15mm
C3	MRI-based Heterogeneous	Cylindrical	(-27, 11, -27)	15mm
H1	Homogeneous Small	Hemispherical	(-15, 0, -12)	15mm
H2	Homogeneous Large	Hemispherical	(24, 3, -17)	15mm
H3	MRI-based Heterogeneous	Hemispherical	(-27, 11, -27)	15mm
P1	Homogeneous Large	Patient Specific	(24, 3, -17)	15mm
P2	Homogeneous Small	Patient Specific	(-15, 0, -12)	15mm
P3	MRI-based Heterogeneous	Patient Specific	(-27, 11, -27)	15mm
P4	Simulation of E1	Patient Specific	(25, 0, -17.3)	16mm
E1	Experimental	Patient Specific	(7, 13, -50.5)	16mm
E2	Experimental with glandular inclusion	Patient Specific	(-28, 12, -31)	16mm

of the breast using the TSAR system [22]. An ultra-wideband (UWB) antenna is scanned around the breast to transmit and collect the reflection data [23]. All numerical breast phantoms are scanned with three different scan patterns: a cylindrical scan pattern; a hemispherical scan pattern; and a patient-specific scan pattern. The scan patterns are shown in Fig. 1-2 and described in detail in [21].

The antenna is excited with a differentiated Gaussian pulse [23]. Reflection data is recorded at 30 azimuth locations around the breast. For each azimuth location, the antenna is moved vertically along the breast and reflections are recorded at 10 equally spaced vertical positions, producing 300 signals. The balanced antipodal Vivaldi antenna with a director in the aperture (BAVA-D) [23] is used to illuminate the breast and record the corresponding reflections. The breast models are simulated using a Finite-difference Time-domain (FDTD) solver. The dielectric properties of breast tissues and immersion liquid are incorporated using Debye models. The Debye parameters are detailed in Table. 2, where ϵ_s is the static permittivity, ϵ_∞ is the permittivity at the limiting frequency, σ_s is the static conductivity and the τ is the relaxation time.

Table 2: Debye Parameters for Numerical Breast Phantoms [21]

Medium	ϵ_∞	ϵ_s	σ_s (S/m)	τ (ps)
Canola oil	2.41	2.52	0.0088	27.84
Skin	32.9	43.6	0.668	77.4
Fat	3.14	4.85	0.036	14.65
Gland (group 1 25th percentile)	9.94	36.5	0.462	10.9
Gland (group 2 50th percentile)	5.73	40.1	0.524	9.15
Gland (group 2 75th percentile)	5.16	51.0	0.766	8.73
Tumour	6.75	56.8	0.794	10.5

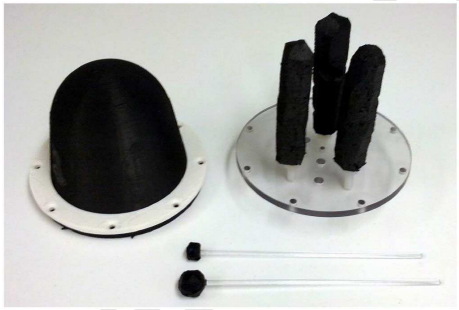

Figure 4: An example of an internal structure configuration attached to a polycarbonate disk (right) to be placed inside a skin layer (left). Two possible tumours attached to polycarbonate rods are shown below(from [24]).

4.2. Experimental Breast Phantoms

4.2.1. Breast Phantom Development

The experimental breast phantoms used in this study have been described in [24]. The breast phantoms include materials representing skin tissue, fatty tissue, glandular tissue and a tumour tissue. A skin layer with 2mm thickness, 10 cm diameter and 9 cm depth (from chest wall to nipple) [13] is created using a skin mould. The skin mould is created with a 3D printer (Replicator 2, MakerBot Industries, Brooklyn, NY) and then filled with a carbon/rubber mixture to create the skin layer.

The internal structures, such as tumour and glandular structures, are also created with a 3D printer and a carbon/urethane rubber mixture is used to create the tumour and glandular structures. The carbon concentration in the carbon/urethane rubber mixture is varied to mimic the dielectric properties of glandular structures and of the tumour. The specific concentrations of carbon/rubber mixture for skin, glandular, tumour and fatty tissues and corresponding dielectric properties are detailed in [24]. The tumour and glandular

structures are glued to nylon threaded rods and bolted to a polycarbonate disk. The polycarbonate disk is then placed inside the skin layer. Fig. 4 shows a skin layer, glandular structures attached to the polycarbonate disk and tumours. The skin layer is then filled with canola oil to mimic the fatty tissue.

Two experimental breast phantoms have been used in this study. The first breast phantom has a skin layer, fatty tissue and a 16 mm diameter tumour located at (7 mm, 13 mm, -50.5 mm) and the second breast phantom contains a skin layer, a 4 cm diameter glandular structure, extending from the tip of the breast to polycarbonate lid, and a 16 mm tumour located at (-28 mm, 12 mm, -31 mm).

4.2.2. Data Acquisition

The measurement data is collected using the prototype system described in [18]. In order to collect the measurement data, the breast phantoms are placed in a tank filled with canola oil. The oil acts as an immersion/coupling liquid. The prototype system has a single BAVA-D [23] antenna that can be positioned around the breast at various azimuth and elevation angles. The prototype has two additional degrees of freedom to control: the proximity and orientation of the antenna relative to the breast skin. For each breast phantom, the antenna is positioned at 7 elevations along the breast depth. For each elevation, measurements are collected at 20 equally spaced positions around the breast. The antenna is positioned 1 cm from the skin and is oriented perpendicular to the skin for each measurement.

A vector network analyzer (PNA-X N5242A or PNA-L N5232A, Agilent Technologies, Santa Clara, CA) is used to collect the measurement data. Measurements are acquired at 1200 frequencies between 10 MHz and 12 GHz with 1 kHz IF bandwidth. The average of 3 measurements is computed [24]. The frequency domain data is then pre-processed before imaging as described in the following subsection.

4.3. Pre-processing

Frequency-domain data is calibrated prior to the application of the artifact removal algorithms and final imaging. The calibration is performed by subtracting measurements which were collected at the same antenna positions but in the absence of the breast phantom. A phase-shift is introduced in the calibrated data to compensate for the antenna aperture location. The calibrated frequency-domain data is then weighted with a differentiated Gaussian pulse of center frequency 4GHz and an approximate bandwidth of 5GHz. Finally, an inverse chirp-z transform [4] is used to convert the frequency-domain data to the time-domain for processing through artifact removal and imaging algorithms.

5. Performance Metrics

In this section the performance metrics are described. The signal analysis metrics are chosen to evaluate the ability of each algorithm to suppress the early-stage skin artifacts and quantify its impact on late-time clutter and tumour

reflections. The image quality metrics have been chosen to measure the quality of images in terms of accuracy of tumour localisation, extent of tumour response and intensity of tumour response.

5.1. Signal Analysis Metrics

5.1.1. Artifact Suppression Ratio

The Artifact Suppression Ratio (ASR) measures the efficacy of the artifact removal algorithm to suppress the early-stage artifact.

The ASR is defined as the ratio of energy of the artifact following and prior to the application of an artifact removal algorithm. The ASR quantifies the energy of residual artifacts after the artifact removal process (that may contribute to the clutter in the images). A high value of ASR indicates larger residual artifacts, whereas lower ASR value indicates that residual artifacts are minimal. The ASR is given as

$$ASR = 10\log\left(\frac{\sum_{n_o}^{m_o}|s[n]|^2}{\sum_{n_o}^{m_o}|b[n]|^2}\right) \tag{8}$$

where $b[n]$ is the backscattered signal prior to artifact removal, $s[n]$ is the signal following artifact removal, and n_o and m_o are the start and end of the artifact-dominant time-window respectively.

5.1.2. Tumour and Clutter Suppression Ratio

The Tumour and Clutter Suppression Ratio (TCSR) measures the impact of the artifact removal process on the energy of the late-time signal which contains tumour and clutter.

TCSR is the ratio of energy of the signal outside the artifact-dominant time-window following, and prior to, the application of artifact removal. A high value of TCSR indicates a minimal effect on the late-time signal whereas a lower value indicates better late-time clutter suppression. TCSR is given as

$$TCSR = 10\log\left(\frac{\sum_{m_o+1}^{N}|s[n]|^2}{\sum_{m_o+1}^{N}|b[n]|^2}\right) \tag{9}$$

where m_o is the end of the artifact-dominant time-window and N is the total length of the time-domain signal.

The late-time clutter is primarily related to the reflections from healthy breast tissues and is often reduced by the artifact removal process. However, the late-time signal also contains the tumour response that is also affected by late-time clutter suppression. The effect on the actual tumour response is measured with another signal metric described in the following subsection.

5.1.3. Tumour Energy Preservation Ratio

The Tumour Energy Preservation Ratio (TEPR) measures the ability of an artifact removal algorithm to preserve the tumour response while removing the artifact.

The TEPR is defined as the ratio of tumour energy obtained from the isolated tumour response ($t_{isolated}[n]$) to the ideal tumour response ($t_{ideal}[n]$). The TEPR is given as

$$TEPR = 10 \log \left(\frac{\sum_{t_1}^{t_2} |t_{isolated}[n]|^2}{\sum_{t_1}^{t_2} |t_{ideal}[n]|^2} \right) \tag{10}$$

where, t_1 and t_2 are the start and end of the time-window containing the ideal tumour response.

The tumour response in artifact removed signals is isolated from late-time clutter by subtracting the artifact removed signals from tumour-bearing and tumour-free phantoms. The ideal tumour response is obtained by subtracting the backscattered signals received from the tumour-bearing and tumour-free breast phantoms.

Ideally, the artifact removal algorithm should not change the tumour response and TEPR should be close to 0 dB. However, in practice, the tumour response is almost always affected and the TEPR quantifies the change introduced in tumour response by an artifact removal algorithm.

5.2. Image Quality Metrics

5.2.1. Full-Width at Half Maximum

The Full-Width at Half Maximum (FWHM) may be used to estimate the extent of the tumour response in the image. The FWHM is defined as the distance from peak tumour intensity to the point where tumour intensity drops by half. The FWHM is computed by growing a region around the centroid of the tumour region until the tumour intensity drops by half. The average Euclidean distance from the centroid of the tumour to the end of the region is estimated to be the FWHM.

5.2.2. Signal-to-Clutter Ratio

The Signal-to-Clutter Ratio (SCR) is used to estimate image quality. The SCR is defined as the ratio of tumour intensity to clutter intensity in the 3D image. The SCR is calculated from the beamformed image obtained following artifact removal.

The overall 3D image is divided into connected regions of different intensity levels present in the image. The highest intensity level region is considered to be the tumour region and the region with the second highest intensity level is considered to be clutter. The extent of both regions is defined by computing the FWHM. The SCR is computed as the ratio of the average intensity in the tumour region to the average intensity of the clutter.

5.2.3. Signal-to-Mean Ratio

The Signal-to-Mean Ratio (SMR) is another measure of the quality of the beamformed image that provides a measure of separation between the tumour intensity and the background clutter. It is defined as the ratio of the average

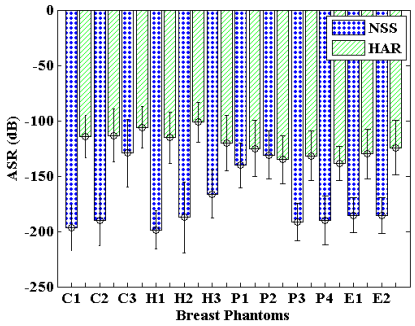

Figure 5: The mean and the standard deviation of Artifact Supression Ratio (ASR) across each breast phantom. The ASR is computed for each radar signal (after processing through both HAR and NSS) of each breast phantom and averaged across each breast phantom. Lower value indicates better artifact suppression.

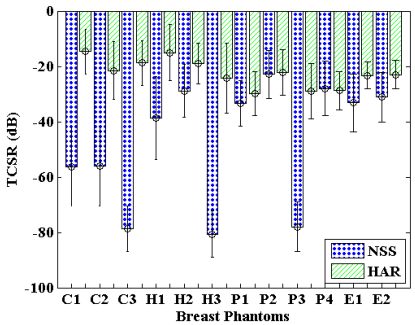

Figure 6: The mean and the standard deviation of Tumour and Clutter Suppression Ratio (TCSR) across each breast phantom. The TCSR is computed for each radar signal (after processing through both HAR and NSS) of each breast phantom and averaged across each breast phantom. Lower values indicate better clutter suppression.

intensity of the tumour region to the average intensity of the overall 3D image. The SMR is also calculated from the beamformed image obtained following artifact removal.

6. Results

6.1. Signal Analysis

6.1.1. Artifact Suppression Ratio

The ASR measures the ability of the artifact removal algorithm to reduce artifacts. The backscattered radar signals from each breast phantom described in Table I are processed through both NSS and HAR algorithms to remove the early-stage artifacts. The ASR is computed for each radar signal and averaged across each breast phantom. Fig. 5 shows the mean and the standard deviation

of ASR computed from each breast phantom following each artifact removal algorithm.

The NSS algorithm demonstrates better artifact suppression capability for all phantoms, including the MRI-based heterogeneous phantom, with significantly lower ASR values compared to the HAR algorithm. However, the average ASR values of the HAR algorithm also remain significantly below 0 dB indicating significant reduction in the artifacts.

Better artifact suppression by the NSS algorithm may largely be attributed to the neighbourhood selection method, where only signals with highly similar artifacts are used to estimate the artifact in a particular channel.

6.1.2. Tumour and Clutter Suppression Ratio

The TCSR evaluates the impact of artifact removal on the late-time signal containing tumour response as well as the clutter due to healthy breast tissues. Fig. 6 shows the mean TCSR of each breast phantom along with the standard deviation computed following both NSS and HAR algorithms.

The relatively lower values of TCSR for the NSS algorithm indicate that the NSS, not only effectively suppresses the artifact but also, reduces the late-time response containing the tumour and clutter. In particular, a significant reduction in the TCSR values by NSS can be observed for heterogeneous breast phantoms (C3, H3, P3). This indicates a significant reduction in energy of the late-time portion of the signals. The HAR algorithm also reduces the late-time response; however on average its impact remains lesser than that of the NSS algorithm.

The neighbourhood selection method of the NSS algorithm provides a group of signals that contains, not only highly similar artifacts but also reflections from interior breast tissues are quite similar. These similar reflections are reduced during the artifact removal process, resulting in lower TCSR values for the NSS algorithm.

The reduction of the late-time response, as indicated by TCSR values, may also result in the reduction of the tumour response. This is due to the fact that the tumour response is also embedded in the late-time response, and may also be reduced by the algorithm, while the late-time clutter is being suppressed.

6.1.3. Tumour Energy Preservation Ratio

The TEPR quantifies the impact of an artifact removal algorithm on tumour energy. The TEPR value is computed for each radar signal after processing through both the NSS and the HAR algorithms and then averaged across the corresponding breast phantom. Fig. 7 shows the mean TEPR computed from each breast phantom along with the standard deviation.

On average, the NSS algorithm has lower values of TEPR. This indicates that it significantly reduces the tumour response. The HAR algorithm also introduces changes in tumour energy; however, the TEPR values for the HAR algorithm, are on average, closer to 0 dB. This suggests minimal change in the tumour response. The standard deviation of TEPR across each breast phantom indicates significant variability. However, this is expected due to the variability

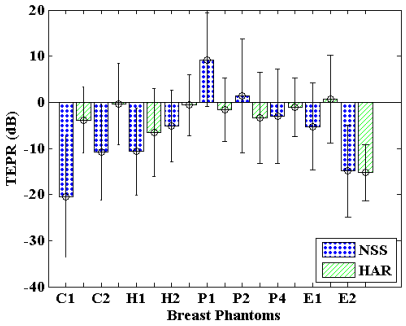

Figure 7: The mean and the standard deviation of Tumour Energy Preservation Ratio (TEPR) across each breast phantom. The TEPR is computed for each radar signal (after processing through both HAR and NSS) of each breast phantom and averaged across each breast phantom. The value closer to 0 dB indicates better tumour response preservation.

in tumour responses received at different antennas. The tumour response received at each antenna is attenuated differently due to the different propagation path. Therefore, the performance of each algorithm varies for each individual signal resulting in variation of the TEPR. In most cases, the HAR algorithm exhibits relatively lower variability compared to the NSS algorithm as shown by the standard deviation.

It is also observed that the tumour energy in some of the signals appears to be greater than the ideal tumour energy. This is due to the imperfect isolation of the tumour response using tumour-bearing and tumour-free phantoms. It is not possible to accurately isolate the tumour response from the response from fibroglandular structures after applying artifact removal algorithms. The TEPR for the heterogeneous phantoms is not calculated for this reason.

In summary, signal metrics such as ASR and TCSR indicate that both algorithms significantly suppress artifacts as well as reduce the late-time clutter. The reduction in the late-time signal also reduces similar reflections from glandular structures within the breast.

However, the NSS algorithm has shown better artifact suppression capability than the HAR algorithm . This is indicated by the lower values of ASR. A better late-time clutter suppression capability of the NSS is indicated by the lower values of TCSR. In contrast, the HAR algorithm has shown better tumour response preservation, as indicated by the TEPR values. The difference between the NSS and the HAR TEPR values may have a significant impact due to the coherent addition of tumour responses at the imaging stage. Therefore, the imaging results must also be analysed to further evaluate the performance of both algorithms.

6.2. Imaging

The artifact free signals are processed through the imaging method described in Section 3 to produce the final images. The following section describes the

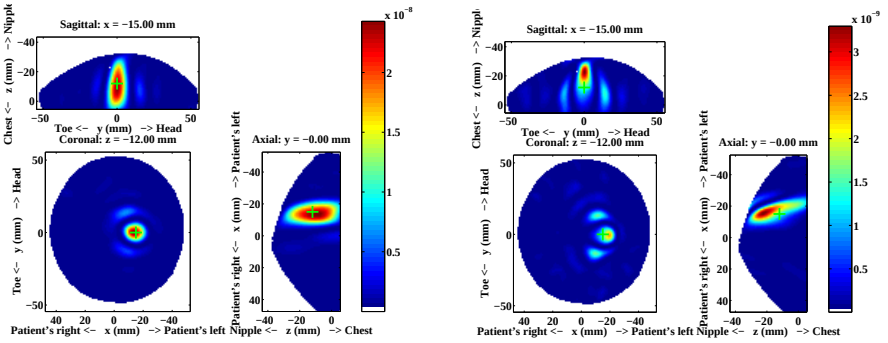

(a) (b)

Figure 8: Beamformed image of C1 following artifact removal using the: (a) HAR algorithm, (b) NSS algorithm.

imaging results and the corresponding imaging metrics computed for each of the breast phantoms.

Table 3: Imaging performance metrics for phantoms scanned with cylindrical scan pattern

Phantom	Algorithm	SCR (dB)	SMR (dB)	Localization Error (mm)	FWHM (mm)
C1	HAR	13.4	35.3	2.2	15.7
	NSS	7.2	34.9	9.0	15.3
C2	HAR	16.5	38.0	4.2	14.5
	NSS	15.6	41.3	6.3	9.7
Average	HAR	14.9	36.7	3.2	15.1
	NSS	11.4	38.1	7.7	12.5

6.2.1. Cylindrical Scan Pattern

Fig. 8 shows the beamformed images of C1 following artifact removal using both HAR and NSS algorithm. The imaging performance metrics, computed from C1 and C2, are presented in Table 3.

The tumour is successfully detected in the images obtained following either artifact removal algorithm. However, localisation error and clutter can also be observed in the images. The HAR algorithm has slightly higher average SCR as well as smaller localisation error compared to the NSS algorithm. However, the average SMR of the NSS algorithm is moderately higher compared to the HAR algorithm.

The difference in performance of both algorithms is somewhat smaller for the C2 phantom. However, the NSS algorithm has lower SCR and higher localisation

error (9.0 mm) compared to the HAR algorithm in the case of the C1 phantom. One contributing factor towards lower performance of the NSS algorithm in the C1 case may be the size of the C1 phantom. The cylindrical scan surface has a fixed radius regardless of the size of the breast. Therefore, the distance between skin and antenna locations in the case of C1 is greater than that for C2 (larger breast phantom). The larger distance results in more attenuated tumour responses from C2 and further attenuation introduced by the artifact removal has a greater impact on the image.

The better SCR and localisation in images of phantoms scanned with cylindrical scan configuration following the HAR algorithm suggests better tumour response preservation compared to the NSS algorithm. However the better average SMR following the NSS algorithm indicates slightly better artifact suppression.

6.2.2. Hemispherical Scan Pattern

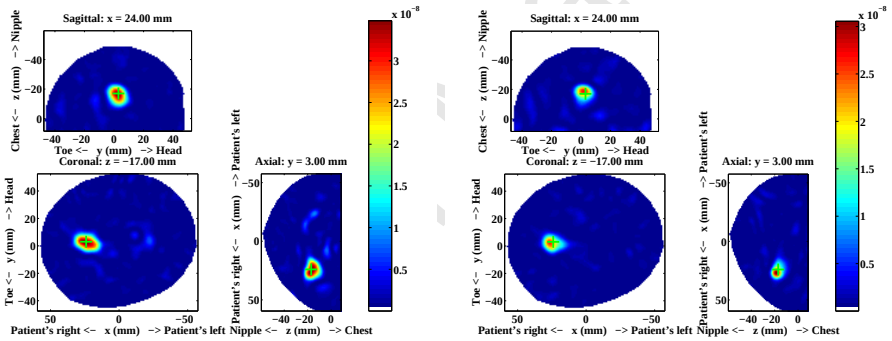

Figure 9: Beamformed image of H2 following artifact removal using the: (a) HAR algorithm, (b) NSS algorithm.

The imaging metrics corresponding to the H1 and H2 phantoms are shown in Table 4. Again, the tumour is detected in both phantom images with small localisation errors using either artifact removal algorithms. The HAR algorithm has, on average, slightly higher SCR and SMR than the NSS algorithm. The average localisation error of the HAR algorithm is also smaller. However, the differences are quite small.

The performance of the HAR algorithm drops in the case of H2. A higher clutter intensity can be observed in the image produced following the HAR algorithm [Fig. 9(a)] compared to the image produced following the NSS algorithm [Fig. 9(b)]. The FWHM of the H2 phantom is also higher for the HAR algorithm indicating smearing of the tumour response. The performance of the HAR algorithm in the case of the H2 phantom may be attributed to the lower artifact suppression. This is shown by the relatively lower ASR value by HAR in the case of the H2 phantom leaving residual artifacts.

Similarly, the performance of the NSS algorithm increases for the H2 phantom. This is again because hemispherical scan configuration is designed to fit H2, which is larger than H1. The neighbourhood-based selection in the NSS algorithm provides a better estimate of the artifact when the hemispherical scan surface fits the breast phantom. This improves the performance of artifact removal.

Table 4: Imaging performance metrics for phantoms scanned with hemispherical scan pattern

Phantom	Algorithm	SCR (dB)	SMR (dB)	Localization Error (mm)	FWHM (mm)
H1	HAR	17.1	38.7	6.1	6.7
	NSS	9.8	33.4	6.1	6.1
H2	HAR	9.9	37.4	3.7	10.7
	NSS	13.6	38.2	4.2	7.3
Average	HAR	13.5	38.1	4.9	8.7
	NSS	11.7	35.9	5.2	6.7

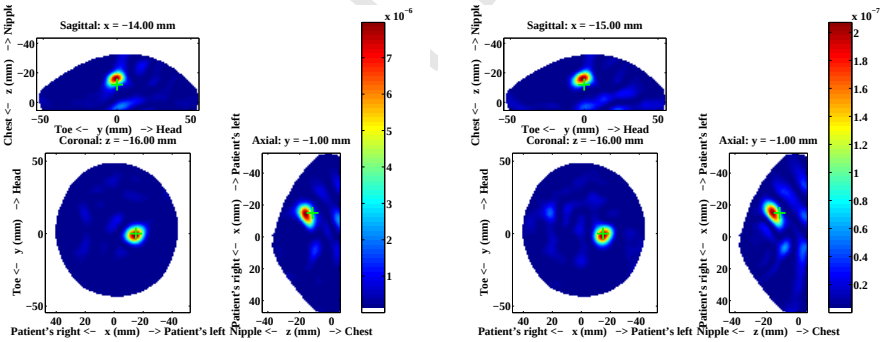

(a) (b)

Figure 10: Beamformed image of P2 following artifact removal using: (a) HAR algorithm, (b) NSS algorithm.

6.2.3. Patient-specific Scan Pattern

Both the HAR and the NSS algorithms, on average, perform similarly in terms of all image quality metrics for the patient-specific scan pattern. This is shown in Table 5.

Fig. 10 shows the image of P2 following application of the HAR and the NSS algorithms. The tumour is quite accurately localised in both images. However, the peak tumour intensity appears to be higher in the HAR image as can be observed in Fig. 10(b).

The higher tumour intensity for the HAR algorithm in this case is attributed to the patient-specific scan pattern, where antennas are placed at approximately constant distances from the skin. Therefore, all antennas located in the same z-plane have highly similar artifacts. This facilitates the HAR algorithm to better remove the artifact while also preserving tumour response.

The scan pattern also benefits the NSS algorithm. This is because the chosen neighbourhood of antennas may provide a better estimate of the artifact due to the higher similarity of skin response. However, it may also have similar response from tumour and interior breast tissues. The response from interior breast tissues may be reduced while subtracting the estimated artifact. Therefore, in this case NSS has a similar SCR to the HAR algorithm even though tumour intensity is lower.

Table 5: Imaging performance metrics for phantoms scanned with patient-specific scan pattern

Phantom	Algorithm	SCR (dB)	SMR (dB)	Localization Error (mm)	FWHM (mm)
P1	HAR	11.5	37.1	2.8	9.9
	NSS	12.2	35.3	2.2	9.0
P2	HAR	12.9	36.4	4.2	7.3
	NSS	12.0	31.3	4.1	8.7
Average	HAR	12.2	36.8	3.5	8.6
	NSS	12.1	33.3	3.2	8.9

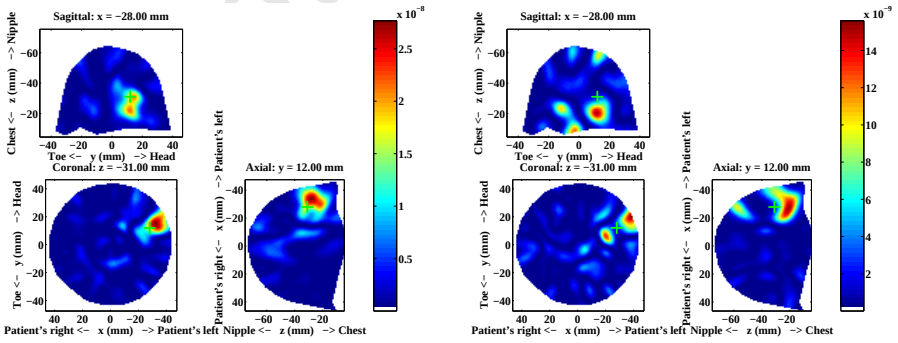

(a) (b)

Figure 11: Beamformed image of E2 following artifact removal using the: (a) HAR algorithm, (b) NSS algorithm.

6.2.4. Experimental Evaluation

For both experimental phantoms, the HAR algorithm performs better in terms of all imaging metrics except for localisation error. This can be seen in Table 6. The average localisation error is marginally higher for the HAR algorithm compared to the NSS algorithm.

The imaging results for the experimental phantom E2 following both artifact removal algorithms are shown in Fig. 11. The tumour is localised in both images. However, the overall clutter, as well as peak clutter intensity, also appears to be higher in the image produced using the NSS algorithm.

The overall imaging performance metrics indicate that the HAR performs better in the case of experimental phantoms. This may be largely attributed to the patient-specific scan pattern.

Table 6: Imaging performance metrics for experimental phantoms

Phantom	Algorithm	SCR (dB)	SMR (dB)	Localization Error (mm)	FWHM (mm)
E1	HAR	12.1	28.5	17.0	19.0
	NSS	6.3	25.9	11.2	15.5
E2	HAR	6.9	27.5	6.5	15.1
	NSS	2.3	27.5	8.1	19.7
Average	HAR	9.5	28.0	11.8	17.0
	NSS	4.3	26.8	9.6	17.6

6.2.5. MRI-based Heterogeneous Phantoms

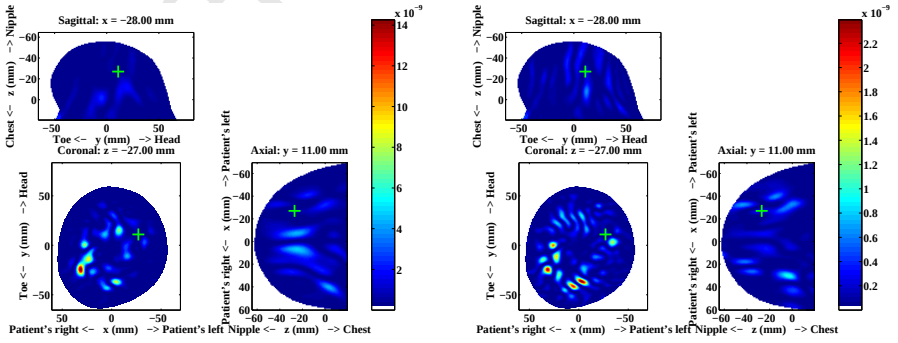

(a) (b)

Figure 12: Beamformed image of C3 following artifact removal using the: (a) HAR algorithm, (b) NSS algorithm.

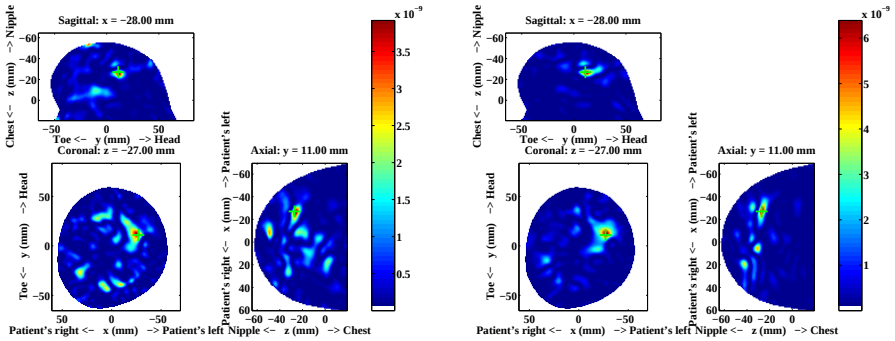

(a) (b)

Figure 13: Beamformed image of H3 following artifact removal using the: (a) HAR algorithm, (b) NSS algorithm.

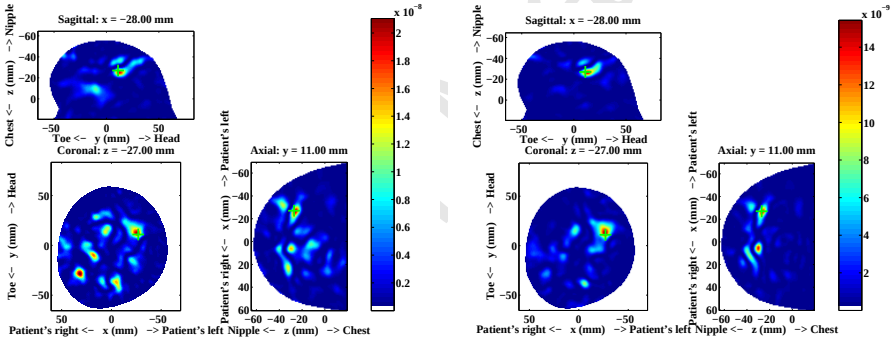

(a) (b)

Figure 14: Beamformed image of P3 following artifact removal using the: (a) HAR algorithm, (b) NSS algorithm.

Fig. 12-14 show the images of MRI-based heterogeneous phantoms obtained after the application of each artifact removal algorithm. The presence of the tumour can be observed in the tumour slices in images of H3 and P3, along with other responses from fibroglandular structures. However, the tumour intensity is weak and clutter is dominant, especially in the images of C3. The cylindrical scan configuration of C3 results in more attenuated tumour reflections due to larger distances between the antennas and the breast. Therefore, the tumour response in the image of C3 is much weaker compared to the clutter response.

The clutter due to fibroglandular tissues is significantly higher in images produced with the HAR algorithm compared with NSS images. The lesser amount of clutter in NSS images is consistent with the signal metric TCSR that indicated a significant reduction in the energy of the late-time portion of the signals for heterogeneous breast phantoms.

The focus of this work is to evaluate the artifact removal algorithms by exclusively quantifying the clutter due to residual artifacts. However, the clutter in the images of the heterogeneous breast is not only associated with the residual artifacts. It may also be attributed to reflections from fibroglandular structures, propagation path inaccuracies and to the ability of the imaging algorithm to suppress incoherent reflections. Therefore, due to ambiguities in identification of the sources of clutter, imaging quality metrics, such as SCR and SMR, are not calculated from the heterogeneous breast phantom. However, the imaging results demonstrate the efficacy of the algorithms in reducing skin reflections from heterogeneous breast phantoms. The results can be improved with more advanced imaging algorithms that have better clutter suppression capabilities such as those reported in [25, 26].

In summary, the HAR and the NSS algorithms have very close average SCR and SMR values for the phantoms scanned with the cylindrical and hemispherical scan pattern. However, the HAR alogrithm has marginally higher average SCR and lower localisation error. The NSS algorithm has an average localisation error almost twice that of the HAR algorithm for the cylindrical scan pattern. This error may be attributed to the distortion introduced by the NSS in the tumour response. However, the NSS algorithm outperforms the HAR algorithm for the hemispherical scan configuration when breast size is similar to the size of the hemisphere used to design the hemispherical scan configuration.

Both algorithms have similar performance in terms of imaging metrics when applied to simulated breast phantoms scanned with the patient-specific scan pattern. However, the HAR algorithm has better performance for the experimental phantoms.

Finally, in the case of the MRI-based phantom, both algorithms reduce the skin-artifacts. However, the strong responses from healthy breast tissues are also present along with the tumour response. The NSS images have less clutter from interior tissues as the NSS algorithm reduces the responses from the interior of the breast in contrast to the HAR algorithm which tends to preserve response from the interior of the breast. Both algorithms are based on the Wiener filter, and therefore the computational complexity of the both algorithms is same. The computational time of the both algorithms is smaller than the overall 3D image reconstruction time of the imaging algorithms [27].

7. Conclusions

In this paper, two promising artifact removal algorithms developed for the radar-based microwave imaging of the breast have been evaluated in various challenging test scenarios. Numerical, as well as experimental, breast phantoms with different tumours included at challenging locations (e.g. close to the skin), and different scan configurations have been used to compare the algorithms. The scan configurations used in this study are the most common configurations used in microwave breast imaging prototypes. Therefore, the results illustrate the potential performance of the both artifact removal algorithms across various prototype systems. Results indicate that both the NSS and the HAR algorithms

effectively reduce the skin-artifacts across all breast phantoms and scan configurations. The responses from interior breast tissues that include healthy as well as cancerous tissues are also reduced by both algorithms. However, the HAR algorithm has been shown to preserve responses from interior breast tissues. In terms of imaging quality metrics, both algorithms produce similar quality images across all scan configurations and simulated phantoms. However, the HAR algorithm produces better quality images for experimental breast phantoms.

It should also be noted that the ability of the NSS algorithm to reduce the responses from the interior breast tissues is particularly useful in heterogeneous scenarios. This is because it facilitates the imaging algorithm to produce images with less clutter due to fibroglandular responses.

Future work will focus on combining these algorithms with advanced imaging algorithms to improve the imaging.

8. Acknowledgment

This work is supported by Science Foundation Ireland (Grant Numbers: 11/SIRG/I2120 and 12/IP/1523), COST Action TD1301, MiMed and the Irish Research Council New Foundations Award. The authors would also like to thank Jrmie Bourqui for scanning the breast phantoms.

References

[1] Xu Li, E. Bond, B. Van Veen, S. Hagness, An overview of ultra-wideband microwave imaging via space-time beamforming for early-stage breast-cancer detection, IEEE Antennas and Propagation Magazine 47 (1) (2005) 19–34. doi:10.1109/MAP.2005.1436217.

[2] E. C. Fear, M. A. Stuchly, Microwave detection of breast tumors: comparison of skin subtraction algorithms, in: C. Nguyen (Ed.), Subsurface Sensing Technologies and Applications II, Vol. 4129, 2000, pp. 207–217. doi:10.1117/12.390618.

[3] E. G. Fear, J. M. Sill, Preliminary investigations of tissue sensing adaptive radar for breast tumor detection, in: Engineering in Medicine and Biology Society, 2003. Proceedings of the 25th Annual International Conference of the IEEE, Vol. 4, IEEE, 2003. doi:10.1109/IEMBS.2003.1280985.

[4] J. Sill, E. Fear, Tissue sensing adaptive radar for breast cancer detection-experimental investigation of simple tumor models, IEEE Transactions on Microwave Theory and Techniques 53 (11) (2005) 3312–3319.

[5] M. Klemm, I. Craddock, A. Preece, J. Leendertz, R. Benjamin, Evaluation of a hemi-spherical wideband antenna array for breast cancer imaging, Radio Science 43 (6).

[6] E. J. Bond, X. Li, S. C. Hagness, B. D. Van Veen, Microwave imaging via space-time beamforming for early detection of breast cancer, IEEE Transactions on Antennas and Propagation 51 (8) (2003) 1690–1705. doi:10.1109/TAP.2003.815446.

[7] W. Zhi, F. Chin, Entropy-Based Time Window for Artifact Removal in UWB Imaging of Breast Cancer Detection, IEEE Signal Processing Letters 13 (10) (2006) 585–588. doi:10.1109/LSP.2006.876346.

[8] A. Maskooki, E. Gunawan, C. B. Soh, K. S. Low, Frequency Domain Skin Artifact Removal Method for Ultra-Wideband Breast Cancer Detection, Progress in Electromagnetics Research 98 (2009) 299–314.

[9] M. A. Elahi, M. Glavin, E. Jones, M. O'Halloran, Artifact removal algorithms for microwave imaging of the breast, Progress In Electromagnetics Research 141 (May) (2013) 185–200.

[10] B. Maklad, C. Curtis, Neighborhood-based algorithm to facilitate the reduction of skin reflections in radar-based microwave imaging, Progress In Electromagnetics Research 39 (February) (2012) 115–139.

[11] M. A. Elahi, A. Shahzad, M. Glavin, E. Jones, M. O'Halloran, Hybrid Artifact Removal for Confocal Microwave Breast Imaging, IEEE Antennas and Wireless Propagation Letters 13 (2014) 149–152. doi:10.1109/LAWP.2014.2298975.

[12] J. Bourqui, E. C. Fear, J. M. Sill, A Prototype System for Measuring Microwave Frequency Reflections from the Breast, International Journal of Biomedical Imaging 2012 (2012) 1–12. doi:10.1155/2012/851234.

[13] E. C. Fear, J. Bourqui, C. Curtis, D. Mew, B. Docktor, C. Romano, Microwave breast imaging with a monostatic radar-based system: A study of application to patients, IEEE Transactions on Microwave Theory and Techniques 61 (5) (2013) 2119–2128. doi:10.1109/TMTT.2013.2255884.

[14] D. Flores-Tapia, O. Maizlish, C. Alabaster, S. Pistorius, Microwave Imaging of Inhomogeneous Breast Phantoms using Circular Hologaraphy, in: Biomedical Imaging (ISBI), 2012 9th IEEE International Symposium on., IEEE, 2012, pp. 86–89.

[15] A. Lazaro, D. Girbau, R. Villarino, Simulated and Experimental Investigation of Microwave Imaging using UWB, Progress In Electromagnetics Research 94 (2009) 263–280. doi:10.2528/PIER09061004.

[16] M. Klemm, I. Craddock, J. Leendertz, A. Preece, D. Gibbins, M. Shere, R. Benjamin, Clinical trials of a UWB imaging radar for breast cancer, Antennas and Propagation (EuCAP), 2010 Proceedings of the Fourth European Conference on (2010) 1–4.

[17] E. Porter, E. Kirshin, A. Santorelli, M. Coates, M. Popovi, Time-Domain Multistatic Radar System for Microwave Breast Screening, IEEE Antennas and Wireless Propagation Letters 12 (2013) 229–232. doi:10.1109/LAWP.2013.2247374.

[18] J. Bourqui, E. C. Fear, Systems for ultra-wideband microwave sensing and imaging of biological tissues, in: Antennas and Propagation (EuCAP), 2013 7th European Conference on, 2013, pp. 834–835.

[19] M. A. Elahi, C. F. Curtis, E. Jones, M. Glavin, E. C. Fear, M. O'Halloran, Detailed Evaluation of Artifact Removal Algorithms for Radar-based Microwave Imaging of the Breast, in: 2015 USNC-URSI Radio Science Meeting (Joint with AP-S Symposium), no. 1, IEEE, 2015, pp. 307–307. doi:10.1109/USNC-URSI.2015.7303591.

[20] T. C. Williams, J. Bourqui, T. R. Cameron, M. Okoniewski, E. C. Fear, Laser surface estimation for microwave breast imaging systems, IEEE Transactions on Biomedical Engineering 58 (5) (2011) 1193–1199. doi:10.1109/TBME.2010.2098406.

[21] D. Kurrant, J. Bourqui, C. Curtis, E. Fear, Evaluation of 3-D Acquisition Surfaces for Radar-Based Microwave Breast Imaging, IEEE Transactions on Antennas and Propagation 63 (11) (2015) 4910–4920. doi:10.1109/TAP.2015.2476415.

[22] J. M. Sill, E. C. Fear, Tissue sensing adaptive radar for breast cancer detection: study of immersion liquids, Electronics Letters 41 (3) (2005) 113–1145. arXiv:0504102, doi:10.1049/el.

[23] J. Bourqui, Balanced antipodal Vivaldi antenna with dielectric director for near-field microwave imaging, IEEE Transactions on Antennas and Propagation 58 (7) (2010) 2318–2326.

[24] J. Garrett, E. Fear, A New Breast Phantom With a Durable Skin Layer for Microwave Breast Imaging, IEEE Transactions on Antennas and Propagation 63 (4) (2015) 1693–1700. doi:10.1109/TAP.2015.2393854.

[25] D. Byrne, M. O'Halloran, E. Jones, M. Glavin, Transmitter-grouping robust Capon beamforming for breast cancer detection, Progress in Electromagnetics Research 108 (July) (2010) 401–416. doi:10.2528/PIER10090205.

[26] M. O'Halloran, E. Jones, M. Glavin, Quasi-Multistatic MIST Beamforming for the Early Detection of Breast Cancer, IEEE Transactions on Biomedical Engineering 57 (4) (2010) 830–840. doi:10.1109/TBME.2009.2016392.

[27] M. A. Elahi, A. Shahzad, M. Glavin, E. Jones, M. O'Halloran, GPU accelerated Confocal microwave imaging algorithms for breast cancer detection, Antennas and Propagation (EuCAP), 2015 9th European Conference on (2015) 1–2.